PCCP

ROYAL SOCIETY OF CHEMISTRY

PAPER

View Article Online
View Journal

Cite this: DOI: 10.1039/d1cp01000j

A new perspective for evaluating the photoelectric performance of organic–inorganic hybrid perovskites based on the DFT calculations of excited states†

Zhengyang Gao,[a] Shengyi Chen,[a] Yang Bai,[a] Min Wang,[a] Xiaoshuo Liu,[ab] Weijie Yang,*[a] Wei Li,[c] Xunlei Ding*[c] and Jianxi Yao*[de]

The high efficiency of organic–inorganic hybrid perovskites has attracted the attention of many scholars all over the world, the chemical formula of which is ABX_3, where A is an organic cation, B is a metal cation, and X is a halogen ion. In addition, the micro-mechanism behind the efficient photoelectric conversion needs more in-depth exploration. Therefore, in this work, based on time-dependent density functional theory (TD-DFT), the electron transfer mechanism from the ground state to the first singlet excited state was systematically investigated by electron and hole analysis and an inter-fragment charge transfer amount method (IFCT). In this work, we optimized and analyzed 99 different perovskite cluster configurations, where A sites are $CH_3NH_3^+$ (MA^+), $NH_2CHNH_2^+$ (FA^+), $CH_3CH_2NH_3^+$ (EA^+), NH_2CHOH^+ (JA^+), NH_3OH^+ (BA^+), $N(CH_3)_4^+$ (DA^+), $CH_3CH_2CH_2NH_3^+$ (KB^+), $CH_3CH_2CH_2CH_2NH_3^+$ (KC^+), $C_3N_2H_5^+$ (RA^+), $CH(CH_3)_2^+$ (TA^+), and $CH_3NH(CH_3)_2^+$ (UA^+), B sites are Ge^{2+}, Sn^{2+} and Pb^{2+}, and X sites are Cl^-, Br^- and I^-. According to the analysis of a series of perovskite clusters of the hole–electron distribution, the distribution is mainly concentrated on BX, and electrons and holes are respectively distributed on B and X sites. The exciton binding energy decreases when the metal element changes from Ge to Pb and the halogen element changes from Cl to I. A radar chart including the exciton binding energy, excited energy, amount of net charge transfer, electron and hole overlap index, distance between the centroid of holes and electrons, and the hole and electron separation index was proposed to intuitively describe the electron transmission characteristics of perovskites. Based on that, a comprehensive score index was innovatively proposed to evaluate the photoelectric property of perovskites, providing foundational guidance for the design of high-efficiency organic–inorganic hybrid perovskites.

Received 5th March 2021,
Accepted 28th April 2021

DOI: 10.1039/d1cp01000j

rsc.li/pccp

1. Introduction

The first application of perovskite materials in dye-sensitized photovoltaic cells has aroused widespread attention in the scientific community.[1] The efficiency of silicon solar cells is close to 25%,[2] which is on the verge of the limited efficiency of semiconductor photovoltaic solar cells based on the detailed balance analysis of photovoltaic physical processes calculated by Shockley and Queisser in 1961.[3] However, the perovskite solar cells can break this restriction. Therefore, carrying out research in this area has great hope for solving the global energy crisis.

A hybrid organometallic perovskite (HOP) can be represented as ABX_3 consisting of three key units, whereby A indicates organic cations such as $CH_3NH_3^+$ (MA^+) or $NH_2CHNH_2^+$ (FA^+), B indicates divalent metal organic cations such as divalent lead cations (Pb^{2+}) or divalent tin cations (Sn^{2+}), and X indicates halides. In the last ten years, many scientists tried their best to

[a] Department of Power Engineering, School of Energy, Power and Mechanical Engineering, North China Electric Power University, Baoding 071003, China. E-mail: yangwj@ncepu.edu.cn
[b] Key Laboratory of Energy Thermal Conversion and Control of Ministry of Education, School of Energy and Environment, Southeast University, Nanjing 210096, China
[c] Institute of Clusters and Low Dimensional Nanomaterials, School of Mathematics and Physics, North China Electric Power University, Beijing, People's Republic of China. E-mail: dingxl@ncepu.edu.cn
[d] State Key Laboratory of Alternate Electrical Power System with Renewable Energy Sources, North China Electric Power University, Beijing 102206, China. E-mail: jianxiyao@ncepu.edu.cn
[e] Beijing Key Laboratory of Energy Safety and Clean Utilization, North China Electric Power University, Beijing 102206, China

† Electronic supplementary information (ESI) available. See DOI: 10.1039/d1cp01000j

improve the photoelectric absorption coefficient of perovskite solar cells (PSCs). In 2009, the photoelectric conversion efficiency of $MAPbI_3$-based solar cells was only 3.8%.[1] The efficiency quickly reached 6.5% by manufacturing $MAPbI_3$ nanocrystals. From 2014 to 2018, the efficiency of PSCs had increased from 13.9% to 23.2%.[4–6] In 2020, the efficiency of perovskite solar cells has reached 25.2%.[7] Perovskites have attracted widespread attention not only because of their high photoelectric conversion efficiency but also because of their powerful adjustability. Each part of ABX_3 is crucial to define the structural and photophysical properties of the perovskite. Giorgi *et al.* compared $MAPbI_3$ with $CsPbI_3$ and found that the lattice parameter shrinkage results in bandgap reduction and also that $CsPbI_3$ has a more powerful hole conductive behavior.[8] When MA^+ is substituted with NH_4^+, the framework PbI_3^- causes the band gap to reduce by 0.3 eV.[9] The electronic states of the anion have a great influence on the observed band gap changes upon halide substitution.[10] For $MAPbI_3$, the X site impacts the valence band energy.[11] When the anion changes from Cl to I, the optical band gap decreases.[12] As the metal cation can directly regulate the band gap, a lead-free perovskite $MASnI_3$ has been successfully synthesised.[13] In short, the strong adjustability of perovskite materials makes people have great expectations for finding an ideal photovoltaic material. Because of the great influence of the photo-excitation process on the solar cell efficiency improvement, exploring the microscopic mechanism of the electronic properties of organometal halide perovskites from an accurate electron transfer point of view is a key point for better exploitation of this class of materials. Unfortunately, research formerly focused mainly on the adjustment of the band gap, while ignoring the exploration of the essential electronic excitation process.

A qualitatively correct description of the electronic band structure of the perovskites may deepen the understanding of the electron transport properties of such materials, supporting the optimization of PSCs. By comparing the femtosecond transient absorption spectra of $MAPbI_3$ in the darkness and under light in an aqueous environment, Christians *et al.*[14] found that humidity has effects on the ultrafast excited-state dynamics of perovskites. In the field of quantitative computing, Umari *et al.*[12] successfully modeled the electronic and optical structure, and transport properties of $CH_3NH_3SnI_3$ and $CH_3NH_3PbI_3$ with the relativistic GW calculations. Park *et al.*[15] comparing the neutral cluster structure of $MAPbI_3$ to the polaron cluster found that the polaron state geometry is more bent and elongated than the neutral geometry. The role of monovalent cations in the process of electronic excitation has also been deeply studied. The orientation of the organic cation has a great influence on the initial force acting on the nuclei in the charge density response.[16] Unfortunately, the role of divalent metal cations and halogen anions was rarely mentioned, which is extremely important for the electron transport process of perovskites. Compared with the periodic model, the cluster model can obtain reasonable calculation accuracy consuming less time.

As the blank research on the electron transfer of perovskite clusters influenced, the transport properties of perovskite clusters have gained our interest. In this work, the micro-mechanism of electron transport of perovskite clusters was researched at a molecular level. In addition, the configuration of the ground state of the perovskite was optimized and the first singlet excited state of the perovskite was analyzed. First, density functional theory calculations were used to get the most stable configuration of the ground state. Second, it is necessary to test the most suitable computational functional and basis set. Third, we studied a series of perovskite cluster models, which are complexes composed of organic cation A^+[$CH_3NH_3^+$ (MA^+), $NH_2CHNH_2^+$ (FA^+), $CH_3CH_2NH_3^+$ (EA^+), NH_2CHOH^+ (JA^+), NH_3OH^+ (BA^+), $N(CH_3)_4^+$ (DA^+), $CH_3CH_2CH_2NH_3^+$ (KB^+), $CH_3CH_2CH_2CH_2NH_3^+$ (KC^+), $C_3N_2H_5^+$ (RA^+), $CH(CH_3)_2^+$ (TA^+), $CH_3NH(CH_3)_2^+$ (UA^+)] and the inorganic anions BX_3^- [B = Ge^{2+}, Sn^{2+}, and Pb^{2+}; X = Cl^-, Br^-, I^-]. In addition, the electron–hole analysis of the first singlet excited state of perovskite was performed. Ultimately, we proposed a descriptor to evaluate the photoelectric properties of perovskites from the novel perspective of electronic excitation. This work can provide a deeper and systematic understanding of the electronic properties of the perovskite to obtain innovative breakthroughs on the band gap adjustment of PSCs and has guiding significance on the commercialization and practical applications for PSCs.

2. Calculation method

Density functional theory (DFT) can provide an accurate result for the geometry and the electronic structure of cluster models. In this work, all calculations were carried out using the Gaussian09 package[17] and ORCA 4.1.1 software.[18] To test which kind of functional is more suitable for the calculation of the excited state of the perovskite, we used the Gaussian09 package to calculate the excitation energy of the testing system with six DFT functionals. Multiple bonding methods form the perovskite, including hydrogen bond and van der Waals (vdW) interactions. Therefore, it is necessary to improve the accuracy of the description of weak interactions. To improving the accuracy of the calculation of the geometric optimization, Grimme's DFT-D3[19] method was used for the correction of dispersion interaction using the Becke–Johnson damping function.[20] We have tested B3LYP,[21] M06-2X,[22] ωB97XD,[23,24] PBE0,[25] CAM-B3LYP,[26] and LC-ωPBE[27,28] to calculate the excited energy of $MAPbX_3$. Here, CAM-B3LYP and LC-ωPBE are the long-range-corrected (LC) exchange functionals. The long-range parameters (ω) of LC-ωPBE were optimized for each test system by using the optDFTω tool.[29] Here, all DFT calculations were calculated with the def2-TZVP[30–32] basis set. For vertical excitation energies, a moderately wide variety of calculations have proved that equation-of-motion coupled-cluster singles and doubles (EOM-CCSD) yield results that are typically within 0.2 eV of experiment for states that are predominantly of single excitation character.[33–37] Whether considering the accuracy or the time cost, ωB2GPPLYP/def2-TZVP has a good performance in calculating charge transition (CT) excited states.[38] Therefore, two different high-precision calculated methods are ωB2GPPLYP[39]/def2-TZVP and EOM-

CCSD/def2-TZVPP.[40–42] The integral approximations (RI)[43–45] have been proven that accelerate the self-consistent field (SCF), and accuracy deviation is acceptable and negligible. ORCA supports the TDDFT calculation with a double hybrid functional and in that ωB2GPPLYP[39] can be calculated with RI technology. Considering that our purpose is to explore a series of perovskite models for comparing the performance differences between different perovskites and qualitatively study their trends, we did not use the solvent model, which may differ from the gas phase.

The hole–electron distribution, which was the difference between the electron density of the first singlet excited state and the ground state, was calculated and analyzed using the wave function analysis software Multiwfn 3.8,[46,47] and the results were visualized using the visualization program VMD 1.9.1.[48] To quantitatively describe the amounts of electrons transferred, the inter-fragment charge transfer (IFCT) method[49] was used to obtain the amount of charge transfer.

We choose 4 indexes to describe the separation of electrons-holes. There is the D index which means the centroid distance of electrons–holes, Sr which represents the overlap of electrons and holes, H index which means the electrons–holes overall average spreading breadth, and t index which can measure whether electrons and holes are significantly separated. These indexes can comprehensively describe the distribution characteristics of holes and charges without losing characteristic information due to the incompleteness of a certain index.

To better understand the electron excitation process, some indices describing electron holes are defined as follows:[47]

$$s(\vec{r}) = \sqrt{\rho^{\mathrm{ele}}(\overrightarrow{r_1})\rho^{\mathrm{hole}}(\overrightarrow{r_2})} \tag{1}$$

where $\rho^{\mathrm{ele}}(\overrightarrow{r_1})\rho^{\mathrm{hole}}(\overrightarrow{r_2})$ are defined as the density of holes and electrons respectively (see more in ref. 47). Then, Sr which means the overlap of holes and electrons is defined as follows:

$$\mathrm{Sr} = \int s(\vec{r})\mathrm{d}\vec{r} \tag{2}$$

The center of mass of the electron (hole) can be calculated using the following formula:

$$X_{\mathrm{ele}} = \int \rho^{\mathrm{ele}}(\vec{r}) \cdot x\mathrm{d}\vec{r} \tag{3}$$

$$\mu_{\mathrm{ele}} = (X_{\mathrm{ele}}, Y_{\mathrm{ele}}, Z_{\mathrm{ele}}) \tag{4}$$

where μ_{ele} (μ_{hole}) means the center of the mass coordinate of the electron (hole), and the calculation method of Y_{ele} and Z_{ele} is the same as that of X_{ele}.

The D index can give the measure of the centroid distance between electrons and holes:

$$\vec{D} = |\mu_{\mathrm{ele}} - \mu_{\mathrm{hole}}| \tag{5}$$

$$D = |\vec{D}| \tag{6}$$

$\overrightarrow{\sigma_{\mathrm{ele}.\lambda}}(\overrightarrow{\sigma_{\mathrm{hole}.\lambda}})$ indicates the distribution breadth of electrons (holes) in the corresponding direction.

$$\overrightarrow{\sigma_{\mathrm{ele}.\lambda}} = \sqrt{(\lambda - \mu_{\mathrm{ele}})^2 \rho^{\mathrm{ele}}(\vec{r})\mathrm{d}\vec{r}} \tag{7}$$

where λ represents the three directions of coordinates (x, y, z).

H_λ measures the average extent of holes and electrons in the λ direction:

$$H_\lambda = \left(\overrightarrow{\sigma_{\mathrm{ele}.\lambda}} + \overrightarrow{\sigma_{\mathrm{hole}.\lambda}}\right)/2 \tag{8}$$

H_{CT} measures the average extent of holes and electrons in the direction of charge transition:

$$H_{\mathrm{CT}} = \left|\vec{H} \cdot \overrightarrow{\mu_{\mathrm{CT}}}\right| \tag{9}$$

where $\vec{H}$ is the vector written together by H_x, H_y, and H_y, and $\overrightarrow{\mu_{\mathrm{CT}}}$ is the unit vector in the direction of charge transition, which can be directly obtained by using the position of the center of mass of electrons and holes (see eqn (4)).

The H index reflects the overall average distribution breadth of electrons and holes:

$$H = \left(\left|\overrightarrow{\sigma_{\mathrm{ele}.\lambda}}\right| + \left|\overrightarrow{\sigma_{\mathrm{hole}.\lambda}}\right|\right)/2 \tag{10}$$

Finally, we define the t index that is used to measure whether electrons and holes are significantly separated as follows:

$$t = D - H_{\mathrm{CT}} \tag{11}$$

If the t index is greater than 0, it implies that the separation of holes and electrons is sufficient, because the centroids of holes and electrons are far away, and their average degree of extension in this direction is relatively not so high.

3. Results and discussion

3.1 Functional testing

Predecessors have tested more than 35 functionals by calculating a series of organic systems of 105 excited states.[69] The results show a clear evolution along with the exact exchange ratio: pure density functionals underestimate the excited energies, whereas hybrids functionals including a large (>50%) share of exact exchange as well as range-separated hybrids suffer from the opposite error. For the calculation of excited states, the proper selection of functionals is a crucial step. Therefore, we compared 6 functionals with 2 more accurate calculation methods. In Fig. 1, when compared with ωB2GP-PLYP/def2-TZVP or EOM-CCSD/def2-TZVPP, M06-2X/def2-TZVP is better than the other tested functionals. In particular, the hybrid exchange–correlation functionals (ωB97XD, LC-ωPBE, and CAM-B3LYP) can improve long-range properties, so that hybrid exchange–correlation functionals are more useful than the traditional hybrid functionals (B3LYP).[26] As we expected, using the LC-ωPBE functional and calculating the ω parameter for each perovskite cluster can improve the accuracy of the excited energy

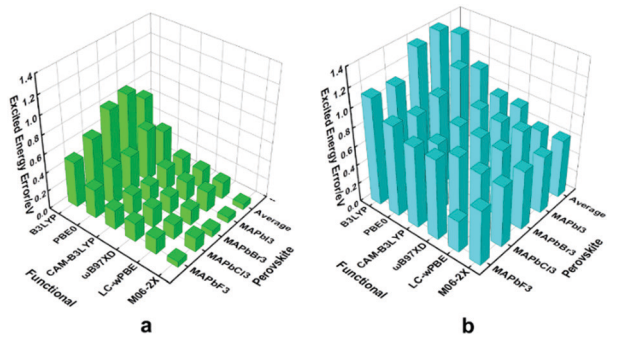

Fig. 1 Comparison of excitation energy calculation errors between six DFT functionals and two high-precision methods: (a) ωB2GP-PLYP/def2-TZVP and (b) EOM-CCSD/def2-TZVPP.

calculation compared to CAM-B3LYP. As has been stated above, M06-2X was chosen as the hybrid functional, and def2-TZVP was chosen as the basis set for the later calculation.

To calculate more accurately, we must consider the accuracy of functionals for the calculation of binding energy between A and BX_3. In Table S3 (ESI†), we test four functionals to compare their binding energy of MA$\cdots$$PbX_3$, using the formula $\Delta E = E_{ABX_3} - E_A - E_{BX_3}$. Besides, we tested four different functionals (M06-2X-D3, M06-2X, B3LYP, and B3LYP-D3). M06-2X can calculate weak interactions when it is proposed, so the calculated binding energy of M06-2X has little change, within 0.007 eV. However, the accuracy of B3LYP for dispersion is very low,[73] and it has the largest error (nearly 0.2 eV) with other functionals in our comparison results. B3LYP-D3 is better than B3LYP and the minimum error is only 0.02 eV. In addition, the time consumption of using DFT-D3 has not increased significantly (Table S3, ESI†). As mentioned above, the DFT-D3 method was used in the later calculation.

3.2 Validation of cluster models

Here, we chose the most studied $MABX_3$ system as the test model, which is shown in Fig. 2(a), and all optimized structures are shown in Fig. S1–S11(a) (ESI†). The bond lengths in the small cluster model may have a great deviation from those of the congener in the bulk crystals. When the B site was determined, the atomic radius of the X site element gradually became larger changing from Cl to I. In the bulk phase model, the skeleton structure which is composed by BX_3 will be affected by other BX_3 in the surrounding environment, but there is no such effect in the cluster model. However, such difference is acceptable. Therefore, according to our calculation results (Table 1), the bond lengths of $MABX_3$ clusters agree well with the experimental data of the crystals, within 7%. Such level of agreement suggests that the isolated cluster model can greatly reflect the properties of bulk materials.[50] Compared with the periodic model, the cluster model can be reliable and more suitable to be applied to research the transport properties of perovskite with a relatively low computing cost.[51–53]

For the hybrid perovskites $MAPbX_3$, whose experimental band gaps are available, we calculated the HOMO–LUMO gaps of their corresponding clusters, as shown in Table 2. The downtrend with the changing from I to Cl has been observed which is consistent with available experimental band gaps and calculated band gaps for bulk materials. By comparing the dependence of the HOMO–LUMO gap and the experimental band gap on X, the curves are almost parallel to each other in Fig. S13 (ESI†). Comparing the band gap calculated by the cluster model and the period model, the average difference is about 5.3 eV. This means that we may use a modified HOMO–LUMO gap, which equals the HOMO–LUMO gap minus 5.3 eV, to compare with the band gap of bulk materials more directly. If we pay attention to the variation in energy band when X changes from I to Cl, we can find that the results of the prediction of the cluster model variation are very close to the experimental results (the largest deviation being about 0.2 eV). This shows that the isolated molecular model can qualitatively characterize the laws of the optoelectronic properties of a series of perovskites at a low cost.

3.3 Separation characteristics of hole–electron pairs

It is crucial for regulating the photoelectric process of perovskites to explore the internal mechanism of the electronic transition process of perovskites. Because of that, the electron transfer properties of $S_0 \rightarrow S_1$ process were analyzed, and the results are shown in Fig. S1–S11 (ESI†) for 99 kinds of organic–inorganic halide perovskites, and those of $MABX_3$ are shown in Fig. 2 as a representative. For $MAPbI_3$, the electrons are distributed on metal cation Pb^{2+} and the holes are distributed on three halide anion I^-. This is the same as the result of the band structure in the period model. The distribution of electrons and holes on Pb $6s^26p^0$ orbital and I $5p^6$ orbital is apparent from the electronic band structure, where the upper valence band is formed from the I p orbitals and the lower conduction band is formed from the unoccupied Pb p orbitals.[10]

To further deeply explore the quantitative difference of a series of perovskites, we calculated the quantitative description parameters of each perovskite S0 $\rightarrow$ S1 excitation, shown in Table S1 (ESI†), and those of $MAPbX_3$ are shown in Table 3 as representatives. The D index means the centroid distance between the holes and electrons. The D index of $MAPbI_3$ is 1.18 Å and the Pb–I bond of $MAPbI_3$ is 2.98 Å, which is nearly 3 times than the D index, which shows that holes and electrons were greatly separated. The Sr index, which ranges from 0 to 1, means the overlap between the holes and electrons, and the larger the Sr index, the more the overlap between electrons and holes. Compared to other perovskites, the holes and electrons of $MAPbI_3$ were separated sufficiently since its Sr value (0.42 a.u.) is less than 0.5 a.u. The H index reflects the overall average distribution breadth of electrons and holes. The H index of $MAPbI_3$ is 2.77 Å, which is larger than $MAPbCl_3$ and $MAPbBr_3$. This indicates that the holes and electrons of $MAPbI_3$ are more widely distributed in space. If the t index is more than 0, it means that the electrons are fully separated from the holes. Compared with those perovskites with the t index less than 0, the t index of $MAPbI_3$ (0.07 Å) is more than 0, so that pairs of electrons and holes were separated adequately. This means that

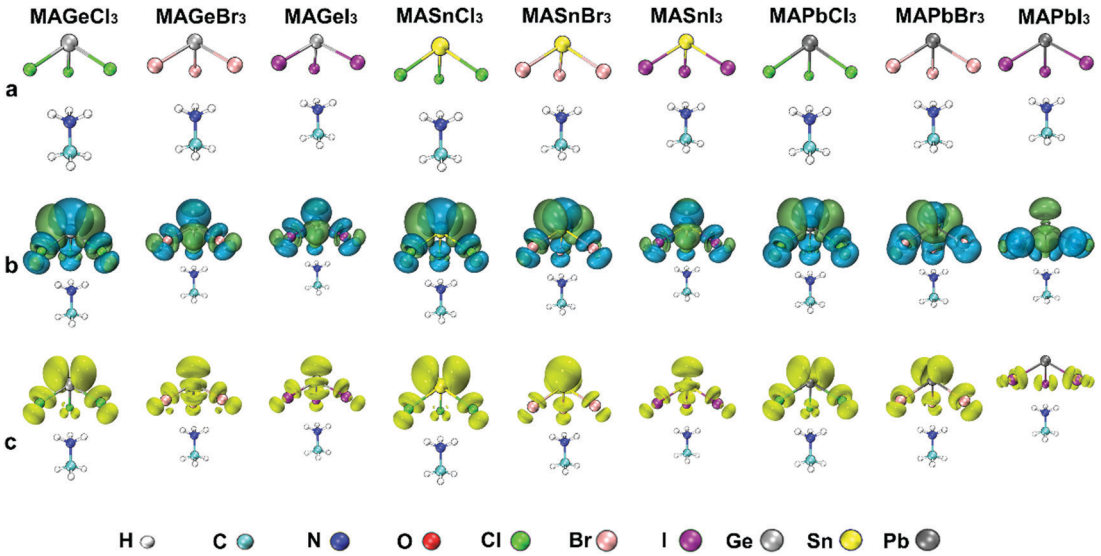

Fig. 2 (a) Structure of $MABX_3$ (B = Ge^{2+}, Sn^{2+}, and Pb^{2+}, and X = Cl^-, Br^-, and I^-). (b) Electron–hole distribution chart. Green and blue isosurfaces represent the distribution of electrons and holes, respectively. (c) $s(r)$ distribution charts. The yellow isosurfaces represent the overlap of electrons and holes. The isosurfaces were uniformly selected as 0.002.

Table 1 Optimized (calc.) bond lengths of the cluster model compared to the available experimental data (exp.) in the bulk crystals of the ambient phase

MA^+	Bond (calc.) (Å)	Bond (exp.) (Å)
C-N	1.48	1.49[54]
C-H	1.09	1.08[55]
N-H	1.03	1.03[55]
BX_3^-	Bond (calc.) (Å)	Bond (exp.) (Å)
Pb–I	2.98	3.2[54]
Pb–Br	2.78	2.98[55]
Pb–Cl	2.61	2.84[56]
Sn–I	2.90	3.05[54]
Sn–Br	2.69	2.89[57]
Sn–Cl	2.52	2.64[56]
Ge–I	2.72	2.77[55]
Ge–Br	2.51	2.53[58]
Ge–Cl	2.34	2.33[56]

Table 2 Calculated HOMO–LUMO gaps of the molecules compared to the band gap calculated by the DFT-GGA-GW with SOC[59] and the experimental values

Molecules	HOMO–LUMO gap (eV)	Band gap (eV)	Exp. (eV)
$MAPbI_3$	6.95	1.67	1.60[60]
$MAPbBr_3$	7.97	2.56	2.39[61]
$MAPbCl_3$	8.69	3.46	3.1[62]

when the X site is I, the electrons and holes always have a more significant separation. To find a more persuasive and universal law, we analyzed the electron excitation results of all optimized structures. The holes and electrons of the perovskite always distribute on the anionic group BX_3^-, as shown in Fig. S1–S11(b) (ESI†). We find the $s(r)$ distribution, which means that the overlap of the electrons and holes became small with the change from Cl to I (see Fig. S1–S11(c), ESI†), and those of $MABX_3$ are shown in Fig. 2(c) as representatives. Furthermore, a more in-depth observation and comparison can find that the separation of electrons and holes is more obvious when BX_3 is PbI_3, that is, the overlap between the two is very small. This indicates that $APbI_3$ has a stronger electronic transmission capacity. We count the amount of the electronic transfer in S0 → S1 between each segment of perovskites by using an Inter Fragment Charge Transfer (IFCT) method. There are three different fragments defined as A, B, and X. For $MAPbI_3$, the net charge transfer from I → Pb is as high as 0.73 e. In addition, the other two direction among charge transfer is MA → Pb (0.00006 e) and I → MA (0.017 e) respectively, which is negligible. This result is consistent with the electron–hole distribution shown in Fig. 2(b). As mentioned above, $MAPbI_3$ has a larger centroid distance of holes and charges (D = 1.18 Å), a smaller overlap area (Sr = 0.42 a.u.), a greater degree of spatial extension (H = 2.77 Å), a higher degree of separation of holes and charges (t = 0.07 Å), and more transmission of charge (Q = 0.73 e). Based on the hole and electron distribution of $MAPbI_3$ reflected by these indexes, we conclude that $MAPbI_3$ has a better electronic performance than other perovskites.

Table 3 Calculation results for the hole-electron distribution index in S0 → S1. D index means the centroid distance between holes and electrons (eqn (6) in Section 2). The Sr index means the overlap between holes and electrons (eqn (1) and (2)). The H index reflects the overall average distribution breadth of electrons and holes (eqn (7)–(10)). The T index measures the degree of separation of holes and electrons (eqn (11))

S0 → S1	D (Å)	Sr (a.u.)	H (Å)	t (Å)
$MAPbCl_3$	0.87	0.67	2.36	−0.41
$MAPbBr_3$	0.96	0.71	2.51	−0.35
$MAPbI_3$	1.18	0.42	2.77	0.07

When a photon is captured by the perovskite, the separating electrons and holes are not directly generated, but an exciton is first generated, which is an electron–hole pair. The binding energy of excitons determines how easy it is to separate electrons and holes. According to the coulombic interactions, we calculated the exciton binding energy using the following formula:

$$E_c = \iint \frac{\rho^{hole}(\vec{r_1})\rho^{ele}(\vec{r_2})}{|\vec{r_1} - \vec{r_2}|} d\vec{r_1} d\vec{r_2} \quad (12)$$

The magnitude of exciton binding energy will ultimately affect the ultimate efficiency of solar cells. According to Table S1 (ESI†), when both A^+ and B^{2+} were determined, exciton binding energy decreased with the changing X site from Cl to I. It is consistent with the previously reported calculation[59] with the periodic model. The downtrend of exciton binding energy is the same as the variation trend of the HOMO–LUMO gap with the change of the X site. From Cl to Br to I, the valence band composition changes from 3p to 4p to 5p with a monotonic decrease in the electron binding energy (lower ionization potential),[10] leading to a lower exciton binding energy in our calculations. Besides, the exciton binding energy decreased with the change in the B site from Ge to Pb, while both A^+ and X^- were determined (Table S1, ESI†). Furthermore, the electronic excitation process of perovskites usually does not participate in organic cation A^+, and holes and electrons are distributed on BX_3^-. When the X site changed from Cl to I, the B–X bond became longer which was the same as that calculated for bulk materials.[59,63] Therefore, the exciton binding energy generated by coulombic interaction has such a tendency to change. Finally, we put a two-dimensional plane fitting diagram (Fig. S14, ESI†). The formula is Es = −1.19 + 0.32Ec + 0.6G, where Es means the excited energy. Ec means the exciton binding energy and G represents the HOMO–LUMO gap. It can be seen from the formula that the excited energy, exciton binding energy and HOMO–LUMO gap of both Ec and G are positively correlated with Es. In addition, R^2 is 0.78, which means that the reliability of this fitting result is acceptable.

3.4 Electron transmission characteristics of perovskites

In the past, the evaluation of the photoelectric performance of perovskites is often based on the perspective of the band gap. In the work, we hope to explore a new way to evaluate the photoelectric performance of organic–inorganic hybrid perovskites from the perspective of electronic excitation. Radar chart is often used to evaluate a certain property with multiple dimensional information. We introduce six characteristic indicators that describe photoelectric properties through different perspectives into the radar chart to prevent the one-sided description of a certain index from causing deviations in the results. Here, we normalize all the characteristic indicators of the excited state of the perovskite and draw it into the radar chart in Fig. 3 (see more data in Table S1 and Fig. S12, ESI†). The normalized values are in the range of [0,1] and the bigger value indicates better photoelectric performance. After linear normalization, these indices have become numerical values, representing that relative magnitudes and various indicators are drawn on the same radar chart to represent the photoelectric properties of materials.

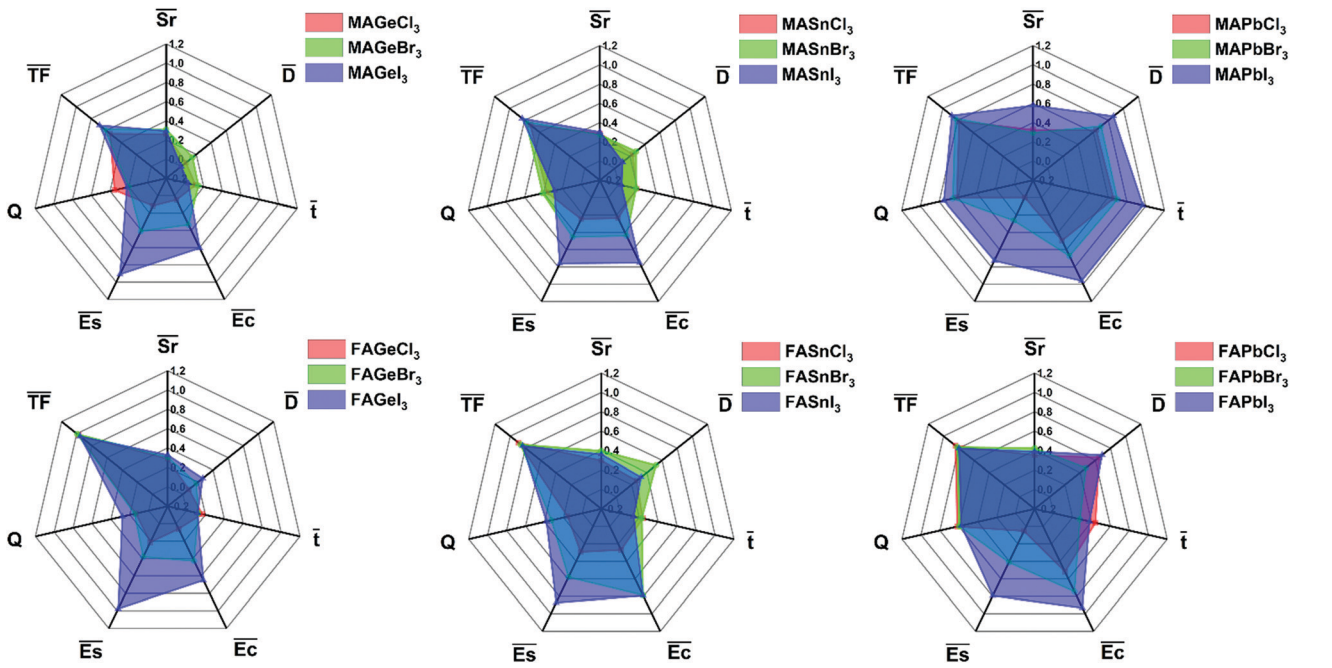

Fig. 3 Radar chart of the normalized electronic excitation characteristic index. The $\overline{Sr}$ index means the separation between holes and electrons. $\overline{TF}$ means the normalized tolerance factor. The Q index represents the net charge transfer. $\overline{Es}$ and $\overline{Ec}$ represent the relative magnitude of excitation energy and exciton binding energy, respectively. The $\bar{t}$ index measures the degree of separation of holes and electrons. $\bar{D}$ index means the centroid distance between holes and electrons.

The larger the area in the radar chart, the better the photoelectric properties of the material. Note that there is still greater approximation in this method because different dimensions have different weights on the final result. The normalized equation of excited energy and exciton binding energy is $X = (\max - x)/(\max - \min)$, $X = (x - \min)/(\max - \min)$ where x is t or D, and $\overline{\mathrm{Sr}} = 1 - \mathrm{Sr}$. We define the sum of the absolute value of the net charge transfer of the three fragments as the total net charge transfer of the perovskite, namely Q. In addition, the maximum value of Q is 1 e, which means that an electron in space is fully excited. The net charge transfer amount does not need normalization. In this way, we plot the evaluation data of the excited state on the radar chart (Fig. 3 and Fig. S12, ESI†). It is found that the area of X = I is always the largest, which indicates the best photoelectric performance, and the change of area shows a trend of I > Br > Cl. The change in the halogen at the X position has little effect on the change of $\overline{\mathrm{Sr}}$, $\bar{t}$ and $\bar{D}$ but it has a great influence on Q, $\overline{\mathrm{Es}}$ and $\overline{\mathrm{Ec}}$. The downtrend of Q, $\overline{\mathrm{Es}}$ and $\overline{\mathrm{Ec}}$ makes the area decrease with the change from Cl to I.

The stability of perovskite is a major problem that hinders the practical application of perovskite solar cells. The tolerance factor[72] (TF) is the most important index to measure the stability of perovskite. When $0.9 < \mathrm{TF} < 1$, a cubic lattice with the highest symmetry and good stability is formed, which is an ideal perovskite structure[70] and for values of TF in the range of [0.78,1.05], perovskite compounds are generally structurally stable.[71] The permutations of 11 different protonated amines, 3 different anionic species, and 3 divalent metal ions lead to 99 TFs. The ionic radius and the tolerance factor are shown in Table S2 (ESI†). Among 99 TFs, 34 TFs ranges from 0.78 to 1.05 such as classic hybrid perovskite $MAPbI_3$ (TF = 0.88), $MASnI_3$ (TF = 0.91), and the series of $BABX_3$ (TF = 0.88–1.01). Therefore, 34 perovskites have a greater possibility to be stable under ambient conditions than the others. Based on the results of TFs, we speculate that $FASnI_3$ and $RAPbBr_3$ (TF = 1.00) could be the most stable structures, while $KBBX_3$ and $KCBX_3$ (TF > 1.1) are most unstable because the A site is too large and the structure cannot maintain the cubic structure. Note that we introduce the tolerance factor into the evaluation index of the radar chart, due to the importance of TF. We hope to find a perovskite with both photoelectric performance and stability. We normalize the tolerance factor as follows: $X = (x - \min)/(\max - \min)$, where $x = |\mathrm{TF} - 1|$.

According to the Shockley–Queisser Limit, the efficiency of single-junction solar cells has a limit value of about 33%. This efficiency value corresponds to a band gap of about 1.34 eV, while perovskite ($MAPbI_3$) is 1.5 eV in the experiment, which is very close to this value. The radar chart evaluation process is based on a basic principle: the larger the area of the polygonal radar chart (S), the better the overall photoelectric performance of the perovskite. Based on the core principle, we propose a score index for each perovskite, which is the area of the polygon in the radar chart. In experiments, the comprehensive index for evaluating perovskite materials often uses power conversion efficiency (PCE). The PCEs of $MAPbI_3$, $MAPbBr_3$, $MASnI_3$, $FAPbI_3$, $FAPbBr_3$, and $FASnI_3$ are 18.61%,[64] 10.40%,[65] 6.40%,[66] 16.38%,[64] 10.00%,[67] and 8.90%.[68] In addition, the score indexes are 1.83, 0.90, 0.53, 1.22, 0.82, and 0.78 (see Table S1, ESI†). The photoelectric performance of the perovskite predicted by the scoring coefficient is in great agreement with that measured by the experimental device ($MAPbI_3$ > $FAPbI_3$ > $MAPbBr_3$ > $FAPbBr_3$ > $FASnI_3$ > $MASnI_3$). There is a good linear relationship between power conversion efficiency and score index in Fig. 4(b), and the fitting formula is $\mathrm{PCEs} = 9.83S + 1.82$. The R^2 is 0.92, which means that the fitting formula is reliable.

We have shown that the modified HOMO–LUMO gap of clusters has a close relationship with the band gap of bulk

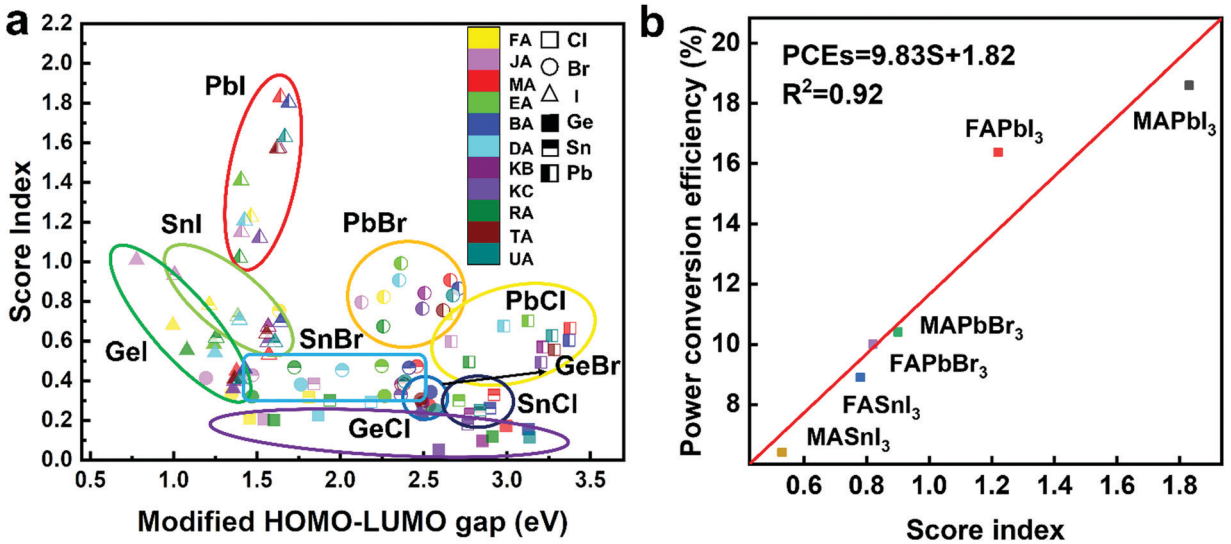

Fig. 4 (a) Electronic excitation characteristic index change trend chart. The different colours of the scattered points represent different A^+, the different filling patterns represent different B^{2+}, and the different shapes represent different X^-. (b) Linear fitting graph of the power conversion efficiency and score index.

materials, which is the most commonly used parameter to measure PCE, so the relationship of S and modified HOMO–LUMO gap is shown in Fig. 4(a). Specifically, the halogen at the X position mainly regulates the magnitude of the modified HOMO–LUMO gap, while the metal element at the B position can control the electronic excitation performance. When halogen elements change from Cl to I, the modified HOMO–LUMO gap becomes smaller and the perovskite can get a higher score while metal elements change from Ge to Pb. Therefore, the photoelectric performance of perovskite is the most excellent when BX_3^- is PbI_3^-. This change rule helps to better adjust the photoelectric properties of perovskites and provides a good guide for experiments.

4. Conclusions

In this work, the excited-state properties of a series of perovskite cluster models were studied by time-dependent density functional theory. According to the functional testing, M06-2X is the most suitable functional to get high-precision computation with a low cost, and cluster models are utilized to study the transport properties of organic–inorganic hybrid perovskites. Stemming from the analysis of a series of perovskite clusters of the hole–electron distribution and inter-fragment charge transfer amount calculation, we analyzed the characteristic parameters describing the first singlet excited state of perovskites. From a novel perspective of excited states, a quantified comprehensive score index is proposed to measure the excellent photoelectric performance of perovskites and we found that the exciton binding energy and scoring index become larger when the metal cation change from Ge to Pb and the halogen anion change from Cl to I. We hope this work can provide a deep insight into the transport properties of perovskites and a guideline for the development and design of efficient perovskite solar cells.

Author contributions

Zhengyang Gao, Dingxun Lei, and Weijie yang conceived and supervised the project. Shengyi Chen wrote the paper. Yang Bai, Min Wang, and Xiaoshuo Liu completed the construction and calculation of the perovskite. Shengyi Chen performed the analysis of the intrinsic properties of the perovskite *via* DFT calculation. Zhengyang Gao, Weijie Yang, Xunlei Ding, and Wei Li put forward constructive comments on the paper. Jianxi Yao provided the foundation. All authors discussed the results.

Conflicts of interest

There are no conflicts to declare.

Acknowledgements

This work was financially supported by the National Key Research and Development Program of China (2016YFA0202401), the National Natural Science Foundation of China (91545122, 61704054), and the Fundamental Research Fund for the Central Universities (JB2015RCY03, JB2019MS052, JB2017MS056). The work was also supported by Beijing Natural Science Foundation (No. 2214064).

Notes and references

1 A. Kojima, K. Teshima, Y. Shirai and T. Miyasaka, *J. Am. Chem. Soc.*, 2009, **131**, 6050–6051.
2 L. G. Gerling, S. Mahato, A. Morales-Vilches, G. Masmitja, P. Ortega, C. Voz, R. Alcubilla and J. Puigdollers, *Sol. Energy Mater. Sol. Cells*, 2016, **145**, 109–115.
3 H. J. Queisser, *J. Appl. Phys.*, 1961, **32**, 1776–1780.
4 N. G. Park, *J. Phys. Chem. Lett.*, 2013, **4**, 2423–2429.
5 R. F. Service, *Science*, 2014, **344**, 458.
6 N. J. Jeon, H. Na, E. H. Jung, T. Y. Yang, Y. G. Lee, G. Kim, H.-W. Shin, S. Il Seok, J. Lee and J. Seo, *Nat. Energy*, 2018, **3**, 682–689.
7 M. A. Green, E. D. Dunlop, J. Hohl Ebinger, M. Yoshita, N. Kopidakis and X. Hao, *Prog. Photovoltaics*, 2020, **28**, 629–638.
8 G. Giorgi, J. I. Fujisawa, H. Segawa and K. Yamashita, *J. Phys. Chem. C*, 2014, **118**, 12176–12183.
9 F. Brivio, K. T. Butler, A. Walsh and M. Van Schilfgaarde, *Phys. Rev. B: Condens. Matter Mater. Phys.*, 2014, **89**, 155204.
10 A. Walsh, *J. Phys. Chem. C*, 2015, **119**, 5755–5760.
11 F. Brivio, A. B. Walker and A. Walsh, *APL Mater.*, 2013, **1**, 042111.
12 P. Umari, E. Mosconi and F. De Angelis, *Sci. Rep.*, 2014, **4**, 1–7.
13 N. Noel, S. Stranks, A. Abate, C. Wehrenfennig, S. Guarnera and A. A. Haghighirad, *Energy Environ. Sci.*, 2014, **7**, 3061–3068.
14 J. A. Christians, P. A. Miranda Herrera and P. V. Kamat, *J. Am. Chem. Soc.*, 2015, **137**, 1530–1538.
15 M. Park, A. J. Neukirch, S. E. Reyes-Lillo, M. Lai, S. R. Ellis, D. Dietze, J. B. Neaton, P. Yang, S. Tretiak and R. A. Mathies, *Nat. Commun.*, 2018, **9**, 2525.
16 M. Pazoki and T. Edvinsson, *Phys. Rev. B*, 2019, **100**, 045203.
17 M. J. Frisch, G. W. Trucks, H. B. Schlegel, G. E. Scuseria, M. A. Robb, J. R. Cheeseman, G. Scalmani, V. Barone, G. A. Petersson, H. Nakatsuji, X. Li, M. Caricato, A. Marenich, J. Bloino, B. G. Janesko, R. Gomperts, B. Mennucci, H. P. Hratchian, J. V. Ortiz, A. F. Izmaylov, J. L. Sonnenberg, D. Williams-Young, F. Ding, F. Lipparini, F. Egidi, J. Goings, B. Peng, A. Petrone, T. Henderson, D. Ranasinghe, V. G. Zakrzewski, J. Gao, N. Rega, G. Zheng, W. Liang, M. Hada, M. Ehara, K. Toyota, R. Fukuda, J. Hasegawa, M. Ishida, T. Nakajima, Y. Honda, O. Kitao, H. Nakai, T. Vreven, K. Throssell, J. A. Montgomery, J. E. Peralta, F. Ogliaro, M. Bearpark, J. J. Heyd, E. Brothers, K. N. Kudin, V. N. Staroverov, T. Keith, R. Kobayashi, J. Normand, K. Raghavachari, A. Rendell, J. C. Burant, S. S. Iyengar, J. Tomasi, M. Cossi, J. M. Millam, M. Klene, C. Adamo, R. Cammi, J. W. Ochterski, R. L. Martin, K. Morokuma, O. Farkas,

J. B. Foresman and D. J. Fox, *Gaussian 09, Revision D.01*, Gaussian, Inc., Wallingford CT, 2009.
18 F. Neese, *Wiley Interdiscip. Rev.: Comput. Mol. Sci.*, 2018, **8**, e1327.
19 S. Grimme, J. Antony, S. Ehrlich and H. Krieg, *J. Chem. Phys.*, 2010, **132**, 154104.
20 S. Grimme, S. Ehrlich and L. Goerigk, *J. Comput. Chem.*, 2011, **32**, 1456–1465.
21 P. J. Stephens, F. J. Devlin, C. F. Chabalowski and M. J. Frisch, *J. Phys. Chem.*, 1994, **98**, 247–257.
22 Y. Zhao and D. G. Truhlar, *Theor. Chem. Acc.*, 2008, **120**, 215–241.
23 J. D. Chai and M. Head-Gordon, *Phys. Chem. Chem. Phys.*, 2008, **10**, 6615–6620.
24 J. D. Chai and M. Head-Gordon, *J. Chem. Phys.*, 2008, **128**, 084106.
25 C. Adamo and V. Barone, *J. Chem. Phys.*, 1999, **110**, 6158–6170.
26 T. Yanai, D. P. Tew and N. C. Handy, *Chem. Phys. Lett.*, 2004, **393**, 51–57.
27 O. A. Vydrov and G. E. Scuseria, *J. Chem. Phys.*, 2006, **125**, 234109.
28 J. D. Chai and M. Head-Gordon, *Phys. Chem. Chem. Phys.*, 2008, **10**, 6615–6620.
29 Tian Lu, optDFTw program v1.0, webpage: http://sobereva.com/346.
30 B. Metz, H. Stoll and M. Dolg, *J. Chem. Phys.*, 2000, **113**, 2563–2569.
31 F. Weigend and Phys Chem, *Chem. Phys.*, 2006, **8**, 1057–1065.
32 K. A. Peterson, *J. Chem. Phys.*, 2003, **119**, 11099–11112.
33 J. F. Stanton, J. Gauss, N. Ishikawa and M. Head Gordon, *J. Chem. Phys.*, 1995, **103**, 4160–4174.
34 J. F. Stanton and R. J. Bartlett, *J. Chem. Phys.*, 1993, **98**, 9335–9339.
35 M. Head-Gordon, R. J. Rico, M. Oumi and T. J. Lee, *Chem. Phys. Lett.*, 1994, **219**, 21–29.
36 D. C. Comeau and R. J. Bartlett, *Chem. Phys. Lett.*, 1993, **207**, 414–423.
37 H. Koch, H. J. A. Jensen, P. Jrgensen and T. Helgaker, *J. Chem. Phys.*, 1990, **93**, 3345–3350.
38 D. Mester and M. Kállay, *J. Chem. Theory Comput.*, 2021, **17**, 927–942.
39 M. Casanova-Páez, M. B. Dardis and L. Goerigk, *J. Chem. Theory Comput.*, 2019, **15**, 4735–4744.
40 F. Weigend and R. Ahlrichs, *Phys. Chem. Chem. Phys.*, 2005, **7**, 3297–3305.
41 K. A. Peterson and C. Puzzarini, *Theor. Chem. Acc.*, 2005, **114**, 283–296.
42 C. Hättig and F. Weigend, *J. Chem. Phys.*, 2000, **113**, 5154–5161.
43 J. L. Whitten, *J. Chem. Phys.*, 1973, **58**, 4496–4501.
44 O. Vahtras, J. Alml and M. W. Feyereisen, *Chem. Phys. Lett.*, 1993, **213**, 514–518.
45 B. I. Dunlap, J. W. D. Connolly and J. R. Sabin, *J. Chem. Phys.*, 1979, **71**, 3396–3402.
46 T. Lu and F. Chen, *J. Comput. Chem.*, 2012, **33**, 580–592.
47 Z. Liu, T. Lu and Q. Chen, *Carbon*, 2020, **165**, 461–467.
48 W. Humphrey, A. Dalke and K. Schulten, *J. Mol. Graphics*, 1996, **14**, 33–38.
49 T. Lu, Multiwfn Manual, Version 3.7 (dev), Section 3.21.1, available at: http://sobereva.com/multiwfn/. (Accessed 20 November 2019).
50 H. Fang and P. Jena, *J. Phys. Chem. Lett.*, 2016, **7**, 1596–1603.
51 Z. Gao, X. Liu, A. Li, C. Ma, X. Li, X. Ding and W. Yang, *J. Mol. Model.*, 2019, **25**, 1–11.
52 H. Li, S. Guo, K. Shin, M. S. Wong and G. Henkelman, *ACS Catal.*, 2019, **9**, 7957–7966.
53 H. Li, K. Shin and G. Henkelman, *J. Chem. Phys.*, 2018, **149**, 174705.
54 K. Yamada, K. Mikawa, T. Okuda and K. S. Knight, *J. Chem. Soc., Dalton Trans.*, 2002, 2112–2118.
55 I. P. Swainson, R. P. Hammond, C. Soullière, O. Knop and W. Massa, *J. Solid State Chem.*, 2003, **176**, 97–104.
56 C. Katan, L. Pedesseau, M. Kepenekian, A. Rolland and J. Even, *J. Mater. Chem. A*, 2015, **3**, 9232–9240.
57 F. Hao, C. C. Stoumpos, D. H. Cao, R. P. H. Chang and M. G. Kanatzidis, *Nat. Photonics*, 2014, **8**, 489–494.
58 G. Thiele, H. W. Rotter and K. D. Schmidt, *Z. Anorg. Allg. Chem.*, 1987, **545**, 148–156.
59 E. Mosconi, P. Umari and F. De Angelis, *Phys. Chem. Chem. Phys.*, 2016, **18**, 27158–27164.
60 J. H. Noh, S. H. Im, J. H. Heo, T. N. Mandal and S. I. Seok, *Nano Lett.*, 2013, **13**, 1764–1769.
61 Y. Yang, M. Yang, Z. Li, R. Crisp, K. Zhu and M. C. Beard, *J. Phys. Chem. Lett.*, 2015, **6**, 4688–4692.
62 G. C. Papavassiliou and I. B. Koutselas, *Synth. Met.*, 1995, **71**, 1713–1714.
63 M. Saba, F. Quochi, A. Mura and G. Bongiovanni, *Acc. Chem. Res.*, 2016, **49**, 166–173.
64 Q. Wei, W. Zi, Z. Yang and D. Yang, *Sol. Energy*, 2018, **174**, 933–939.
65 J. H. Heo, D. H. Song and S. H. Im, *Adv. Mater.*, 2014, **26**, 8179–8183.
66 N. K. Noel, S. D. Stranks, A. Abate, C. Wehrenfennig, S. Guarner, A. A. Haghighirad, A. Sadhanal, G. E. Eperon, M. B. Johnston, A. M. Petrozz, L. M. Herz and H. J. Snaith, *Energy Environ. Sci.*, 2014, **7**, 3061–3068.
67 F. C. Hanusch, E. Wiesenmayer, E. Mankel, A. Binek, P. Angloher, C. Fraunhofer, N. Giesbrecht, J. M. Feckl, W. Jaegermann, D. Johrendt, T. Bein and P. Docampo, *J. Phys. Chem. Lett.*, 2014, **5**, 2791–2795.
68 X. Meng, J. Lin, X. Liu, X. He, Y. Wang, T. Noda, T. Wu, X. Yang and L. Han, *Adv. Mater.*, 2019, **31**, 1903721.
69 D. Jacquemin, B. Mennucci and C. Adamo, *Phys. Chem. Chem. Phys.*, 2011, **13**, 16987–16998.
70 G. Kieslich, S. Sun and A. K. Cheetham, *Chem. Sci.*, 2014, **5**, 4712–4715.
71 S. A. T. Redfern, *J. Phys.: Condens. Matter*, 1996, **8**, 8267.
72 V. M. Goldschmidt, *Naturwissenschaften*, 1926, **14**, 477–485.
73 J. Witte, M. Goldey, J. B. Neaton and M. Head-Gordon, *J. Chem. Theory Comput.*, 2015, **11**, 1481–1492.